AD-A267 615

INT. J. REMOTE SENSING, 1993, VOL. 14, NO. 7, 1305-1324

DTIC
ELECTE
AUG 04 1993
S A D

Observation of flooded ice in Arctic regions

A. K. GOROCH and R. W. FETT

Naval Research Laboratory,[1] Marine Meteorology Division, Monterey, CA 93943-5006, U.S.A.

93-17335

(Received 21 March 1991; in final form 20 March 1992)

Abstract. The remote detection of flooding in the Arctic ice pack has been difficult to accomplish using conventional techniques. We have examined a case of Artic flooding (8 June 1989) with NOAA and DMSP visible and infrared measurements supplemented by DMSP microwave imager (SSM/I) data. Analysis of visible and infrared data for a sunglint region was used to show the distribution of flooding at 72° N, 135° W. A simple model was developed for the radiative transfer at microwave wavelengths through a bring layer over ice. The predictions of the model were found to be consistent with the spatial behaviour of the SSM/I measurements. This case study demonstrates the usefulness of using combine visible, infrared, and microwave measurements to differentiate among flooded, broken ice, and open water regions, even in the presence of cloud cover or surface fog.

1. Summary

Changes in size and physical characteristics of the polar ice caps are an important mechanism controlling global climatic change. The freezing and melting of the ice surface affect both the thermodynamic balance and the mechanical structure of the ice cover. Naval and marine operations in the polar regions depend on the knowledge and forecasting of ice cover and open water occurrence.

The surface melting of ice is an important component of the dynamics of ice surface change. The surface melt provides a thermodynamic reservior for solar heating, and as such is critical to the analysis and forecast of polar ice growth and breakup. In this work we use conventional optical (visible and infrared) imagery with passive microwave measurements to investigate the occurrence of Arctic melt ponds.

The extent of ice cover in the Arctic is conventionally determined by examination of cloud free visible imagery. However normal inspection of such data does not determine whether the ice is flooded or free of surface water. A more detailed analysis of such data, however, may provide evidence of water on the ice surface. Sunglint, not normally considered over ice covered regions, is valuable in determining extent of flooding. Multi-spectral comparison of the near-infrared channel measurements may reveal a darkening over a water covered ice surface, since water is essentially black in the infrared.

Microwave data add a further dimension to the differentiation of flooded and non-flooded regions. The microwave emissivity of water and ice differ substantially, providing an effective means for differentiating ice from sea water in polar regions.

[1] Formerly Naval Oceanographic and Atmospheric Research Laboratory.

0143-1161/93 $10.00 © 1993 Taylor & Francis Ltd

This document has been approved for public release and sale; its distribution is unlimited.

93 8 3 048

DISCLAIMER NOTICE

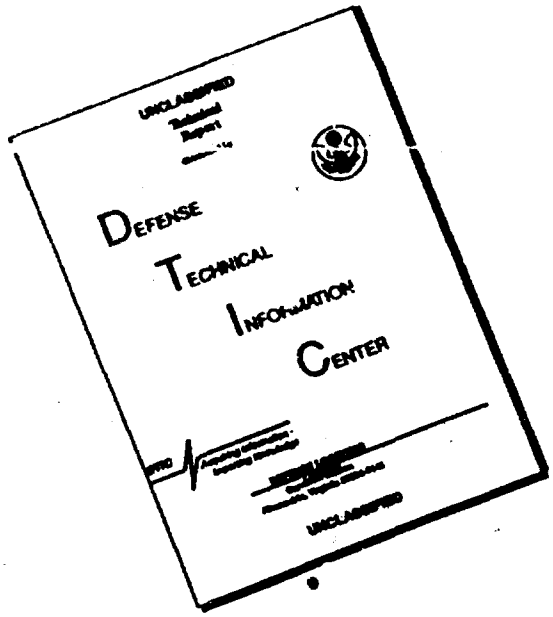

THIS DOCUMENT IS BEST QUALITY AVAILABLE. THE COPY FURNISHED TO DTIC CONTAINED A SIGNIFICANT NUMBER OF PAGES WHICH DO NOT REPRODUCE LEGIBLY.

In the case of water layers on the ice surface, the microwave surface emission depends on wavelength, so that a thin layer of water may emit like water at high frequencies and like ice at low frequencies. Thus, a multiple frequency microwave radiometer, such as the SSM/I microwave imaging sensor on the DMSP F-8 satellite has the potential to evaluate physical properties of melt pond regions. In this work we investigate water covered ice surfaces, and determine the potential of determining ice pond characteristics from this wavelength dependence.

Visible imagery has been used previously to determine extent of ice flooding and pond formation. During sun glint conditions, the surface exhibits strong reflection compared to either an open water region or an ice covered region. We use DMSP Operational Line Scanner (OLS) and NOAA-8 AVHRR imagery to determine ice pond areas from sun-glint effects. The physical characteristics of the ponds are then investigated using SSM/I observations.

A simple model of microwave emission from a water covered surface is described, accounting for features observed in the microwave observations. This model indicates the expected wavelength dependence of microwave emission by the surface. The scatter plots of 19 and 37 GHz channels are shown to provide differentiation between ice and melt pond regions. This expectation is verified in the visible and infrared imagery. The results suggest that spatial textural analysis may be a useful technique of analyzing microwave observations in the Arctic.

2. Introduction

The conditions of the surface in polar region have an important effect on global scale thermodynamics, as well as being critical for the analysis and forecast of weather. The surface is complicated, consisting of ice and liquid water and various combinations of the two forms of water substance, together with various concentrations of salt. The complexity of the surface makes it difficult to reliably infer conditions from conventional observations such as visible or infrared satellite imagery, and implies the need to use additional measurements.

A particular example of this complexity occurs in regions of surface ice melt ponds. These areas are formed as a result of solar heating of ice and generally characterized by thin layers of water interspersed among solid ice regions. Because the liquid is a vehicle for transport of salt from the ice, these regions are thought to be responsible for the transformation of ice from higher salinity first year forms to lower salinity multi-year forms (Comiso 1983, Comiso *et al.* 1984).

Ice pond formation is often observed during the onset of solar summer (figure 1). The characteristics of the ice ponds vary: size and depth depend on the incident solar flux, ice salinity, and ice roughness. The ice ponds are observed in visible satellite imagery when satellite and solar geometry permit the detection sun glint (Fett and Rabe 1976).

3. Satellite measurements

3.1. *Microwave sensor characteristics*

The DMSP SSM/I sensor is a passive microwave imager deployed aboard the DMSP F10 satellite. The satellite operates in a circular sun-synchronous orbit at an altitude of 833 km with an inclination of 98·8°, and an orbital of 102·0 minutes. The SSM/I is a passive microwave radiometer operating at four frequencies with two polarizations as seen in table 1 (Hollinger *et al.* 1987).

The SSM/I data are sampled to provide effective temperatures over a nominally

Figure 1. Representative flooded ice region in the arctic (courtesy of Defense Research Board, Canada, WMO/OMM/BMO – No 259, TP. 145)

Table 1. DMSP SSM/I sensor characteristics.

Channel	Frequency (GHz)	Wavelength	Polarization
1	19·35	1·55	Vertical
2	19·35	1·55	Horizontal
3	22·235	1·35	Vertical
4	37·0	0·81	Vertical
5	37·0	0·81	Horizontal
6	85·5	0·35	Vertical not operational
7	85·5	0·35	Horizontal

25 km square region for channels 1–5, and 12·5 km for channels 6 and 7. The sensor rotates about an axis parallel to the spacecraft vertical at an angle of 45 from the vertical. Brightness temperatures are measured over an angular sector from −51·2 to 51·2° about the aft direction (Hollinger *et al.* 1987).

These data are received at the Fleet Numerical Oceanography Center (FNOC) for operational product development. The raw data are earth located and stored as temperature data records (TDRs). The TDRs are the corrected for antenna pattern effects and stored as Sensor Data records (SDRs). The SDRs are then used with geophysical algorithms to provide Earth located environmental data records (EDRs), including water vapour column concentration, precipitation, and ocean surface wind speed. The SSM/I SDRs, TDRs, and EDRs are forwarded to the Naval Research Laboratory (NRL) for archival. The data used here are SDRs obtained from the NRL archives.

3.2. *Visible and infrared satellite sensor characteristics*

The optical measurements used in this study are taken by the Operational Line Scanner (OLS) and the DMSP satellite, and the Advanced Very High Resolution

DTIC QUALITY INSPECTED 3

A-1 20

Radiometer (AVHRR) deployed aboard the NOAA-9 satellite. The operation line scanner is an visible and infrared imager deployed aboard the DMSP F-8 space craft. The instrument scans a swath 2200 km in width at the satellite subpoint, and in the direction perpendicular to the satellite motion vector. The instrument operates with two resolutions, 2·5 km and 0·6 km. The sensor produces images in the visible band, from 0·4 nm to 1·1 nm, and the infrared band, nominally from 8 nm to 12 nm.

The AVHRR is a five channel optical sensor including two visible channels, one middle infrared channel, and two thermal infrared channels. The instrument scans a swath 2200 km in width at the satellite subpoint. The resolution of the sensor is nominally 1000 m at satellite subpoint. The channel characteristics of both sensors are provided in table 2.

4. Emissivity of the Artic surface

The microwave properties of the polar surface have been modelled by several investigators (Isaacs *et al.* 1989, Comiso 1983, Grody 1988). It is generally agreed that microwave emission can be used to differentiate among five surface types; clear water, multi-year ice, single year ice, water covered ice, and snow covered ice.

Clear water is characterized by a high microwave dielectric coefficient, and a correspondingly low emissivity, on the order of 0·5. Brightness temperature is cold, although this is a function of salinity, temperature, and physical surface structure as well. Because of the low emissivity, most of the microwave radiance from the water surface emanates from within one or two wavelengths below the surface.

First year ice consists of an ice matrix with interstitial brine pockets. The brine pockets increase the dielectric coefficient and emissivity of the pure ice; thus the first year ice T_b, is warmer than that of a water surface, but colder than pure ice. Associated with the higher emission, the emitted radiance emanates from deeper below the ice boundary than water.

Multi-year ice has undergone multiple melt cycles, in which interstitial brine has been drained away and effectively replace by air pockets. Density is lower than that of first year ice, and as Comiso points out, the lower density has two effects on microwave emission. First, there is less emitting material per layer of ice, and second, the air pockets in the ice scatter the incoming radiation. The effective T_b at a given physical temperature is therefore relatively lower than for first year ice. The difference between first year and multi-year ice are shown in figure 2.

Table 2. Visible and infrared sensor characteristics.

Band	Channel	Frequency (nm) band	Ground resolution (km)
DMSP			
Visible	1	0·4–1·1	0·6–2·5
Thermal	2	8·0–12·0	0·6–2·5
NOAA AVHRR			
Visible	1	0·58–0·68	1·1
Near-infrared	2	0·725–1·1	1·1
Mid-infrared	3	3·55–3·93	1·1
Thermal 1	4	10·5–11·5	1·1
Thermal 2	5	11·5–12·5	1·1

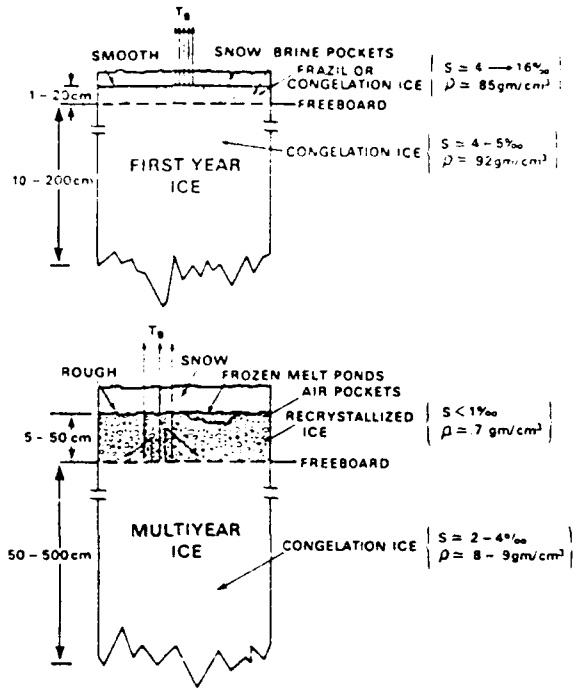

Figure 2. Physical characteristics of first year and multi-year ice (Comiso 1983).

Brine melt on the ice surface has not been studied extensively (Cavalieri *et al.* 1983, Svendsen *et al.* 1983, Garrity *et al.* 1990). As seen in figure 1, the ice surface is covered with liquid of varying depth from relatively thin layer to thick. The extent and thickness of the liquid layer depends on the extent of solar heating, the porosity of the ice, and other physical characteristics.

The physical characteristics of the layer affect the microwave emission characteristics of the surface. If the liquid is greater than the skin depth of the microwave radiation, the primary emitted radiation component comes from the water, and consequently is relatively cold. If the liquid depth is less than the skin depth, the underlying ice layer contributes to the total emitted radiation from the surface, and the surface will seem to be emitting as a warmer equivalent temperature. The following paragraph provides a quantitative description of the transfer of microwave radiation in the flooded ice system. While this simple model does not include reflection at the air-brine interface, it seems sufficient to demonstrate the salient points of the observed data.

5. Microwave emission of a flooded ice surface

The radiance emitted at the air-liquid interface (figure 3) is described by the radiative transfer equation in the zenith direction (Ulaby *et al.* 1986, Simmer 1989),

$$\frac{\delta I}{\delta z} = -kI + KS \tag{1}$$

where I is the radiance at any point in the liquid layer, k is the local absorption coefficient, and S is the source function. The solution for the case of plane parallel system with an ice boundary under a layer of water is

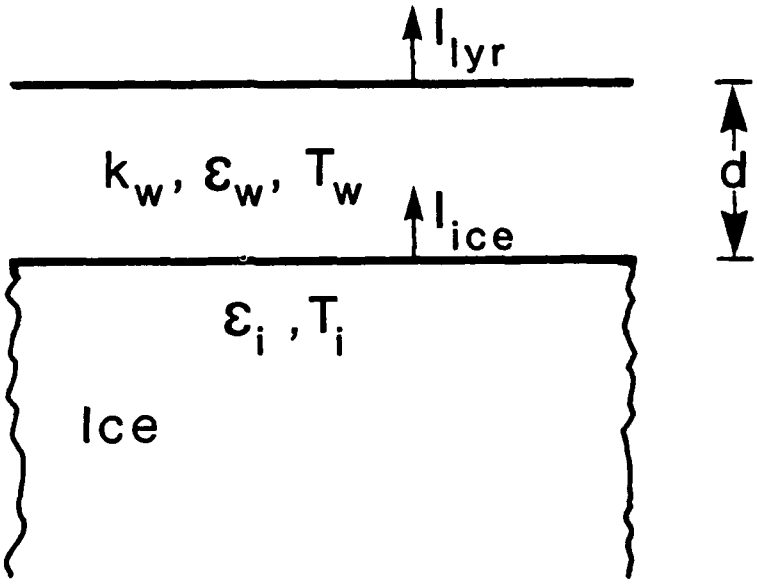

Figure 3. Physical model for radiative transfer through a flooded ice surface.

$$I = I_{ice} e^{-kz_{liquid}} + \int_0^{z_{liquid}} e^{-kz'} S(T) dz' \tag{2}$$

The water is assumed to be homogeneous, so the source term is independent of z, and may be removed from inside the integral. The upward radiance at the top of the liquid layer is

$$I = I_{ice} e^{-\tau_{water}} + S(T)(e^{-\tau_{water}} - 1) \tag{3}$$

In the microwave the Rayleigh-Jeans approximation is valid, so the Planck function may be linearized as follows

$$S_\nu = \left(\frac{2h\nu^3}{c^2\left(e^{\frac{h\nu}{kT}} - 1\right)} \right) \approx 2kT\left(\frac{\nu}{c}\right)^2 \tag{4}$$

The radiance is conventionally related to the brightness temperatures by

$$T_B = \frac{c^2 I}{2k\nu^2} \tag{5}$$

The brightness temperature observed above a layer of surface water is then

$$T_B = e^{-\tau_{lyr}} T_{Bice} + (1 - e^{-\tau_0}) T_{Bwtr} \tag{6}$$

The brightness temperature of the surface is related to the surface emissivity and the physical temperature of the system. The general equation of the perceived brightness temperature of a water covered surface with ice at one temperature and water another temperature is

$$T_B = \varepsilon_{ice} e^{-\tau_0} T_{ice} + \varepsilon_{wtr}(1 - e^{-\tau_0}) T_{wtr} \tag{7}$$

The emissivity of ice and sea water are calculated using parametrizations summarized in Appendix A.

The brightness temperature at any microwave frequency will be a function of the relationship of the brine layer depth and the microwave frequency. Thin layers of water will affect the higher frequency emissions rather strongly, while lower frequencies are unaffected. We have calculated the effective brightness temperature of a solid ice structure covered with a thin layer of brine, with a salinity of 34 per thousand, identical to sea water. (The salinity of the melt region may in fact differ from this value, but the results of the analysis remain unchanged). Figure 4 shows the dependence of the microwave brightness temperature on the water depth for the microwave frequencies used by the SSM/I.

This figure implies that the variation of the brightness temperature of a brine surface depends both on the layer depth and the microwave frequency. If the brine layer depth is on the order of millimetres thick, the long wavelength brightness temperature (19 and 22 GHz) will be unaffected, while the shorter wavelengths will vary depending on the areal extent and depth of the brine cover. Thus, the long wavelength T_b is expected to have a smaller variance over a small region, than the shorter wavelength. On the other hand, if the layer depth is on the order of a centimetre, the short wavelength emission will be primarily from the brine layer, while the longer wavelength signal is attributable to the relatively hot ice emissions, modified by the absorbing water layer. Since the brine layer is not uniform, it is

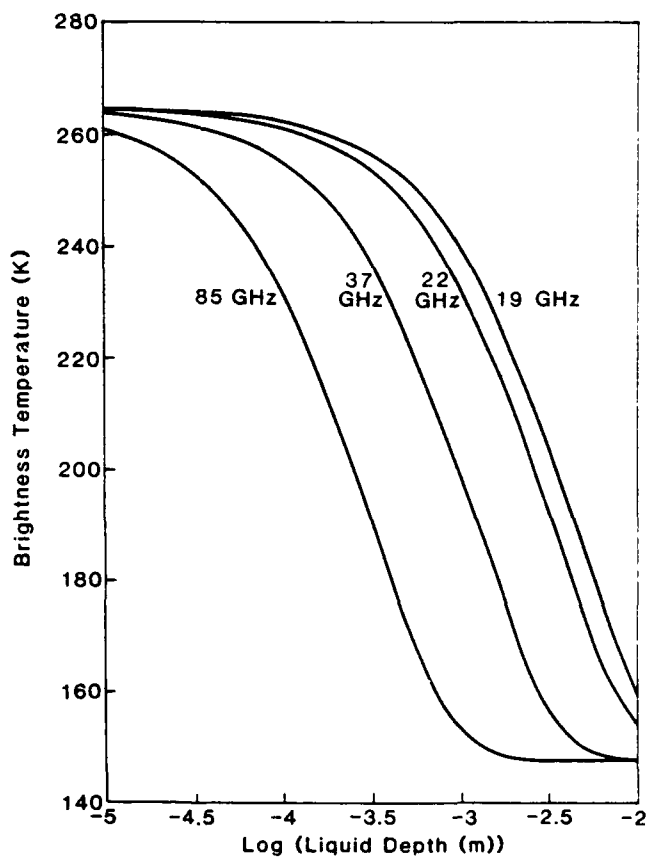

Figure 4. Microwave brightness temperature as a function of liquid depth and frequency.

expected that the longer wavelength will then vary more than the shorter wavelength.

The sensitivity of the brightness temperature observations to brine depth can be demonstrated by observing the derivative of the brightness temperature with respect to the liquid depth. A graph of the sensitivity of the brightness temperature to liquid depth is shown in figure 5. The higher frequencies show a maximum sensitivity when the liquid layer is thinnest. As the layer thickness increases, the lower frequencies become more dominant. Note however, that the depth sensitivity at low frequencies is less than that for high frequencies and thin liquid layers. When we consider a small region which would have a distribution of liquid depths, the brightness temperature will vary depending on the details of the distribution, as well as the relation between the microwave frequency and the liquid depth. From figure 5, we would expect the maximum variation of brightness temperature to be at high frequencies, when the layers are quite thin, possibly less than the skin depth, with lower frequencies not showing the same extent of variation.

6. Observations of Artic flooded regions

We have collected both visible and microwave measurement of an apparently flooded region in the Beaufort Sea north of the Mackenzie River Delta (65° N, 122° W). The region consists of open water, first year and multi-year ice, and ice pond regions. Visible and microwave measurements provide the capability of

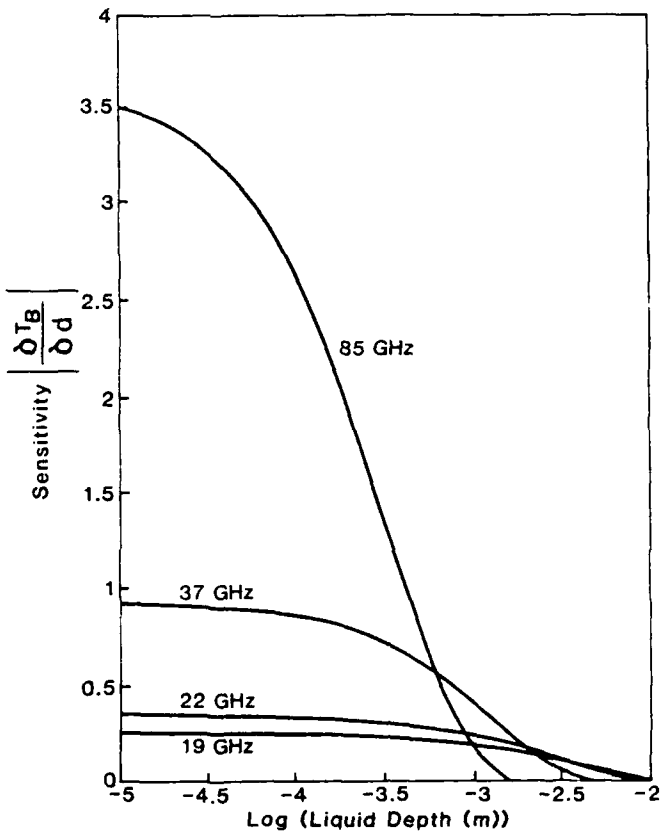

Figure 5. Sensitivity of brightness temperature to liquid depth.

evaluating different physical characteristics of the ice cover. The following sections analyse surface features from the optical and the microwave data.

6.1. *Analysis of visible and infrared imagery*

Figure 6 is a DMSP visible high resolution (550 m) image showing the region on 8 June 1989, at 1820 UTC. A band of fast ice approximately 55 km in width is apparent just north of the delta. Reflectivity within the band is not constant, suggesting the possibility of ice of variable thickness, age, or surface characteristics. The band of ice is rimmed on the northern side by another narrow band of open water (or thin ice-covered water).

To the north of these features lies the ice pack or drift ice of the Beaufort Sea. The area shown is west of Banks Island, extending in the direction of Point Barrow along the North Slope of Alaska. Normal southward drift of the ice pack west of Banks Island caused by the anticyclonic gyre in the Beaufort Sea and prevailing high pressure over the region has created a shear zone between the fast ice on the west coast of Banks Island and the ice pack. A flaw polynya or flaw lead appears in that region. Numerous large and small broken elements of ice cover the area and extend southward into the Amundson Gulf.

Figure 6. DMSP high resolution visible image, 8 June 1989, 1820 UTC.

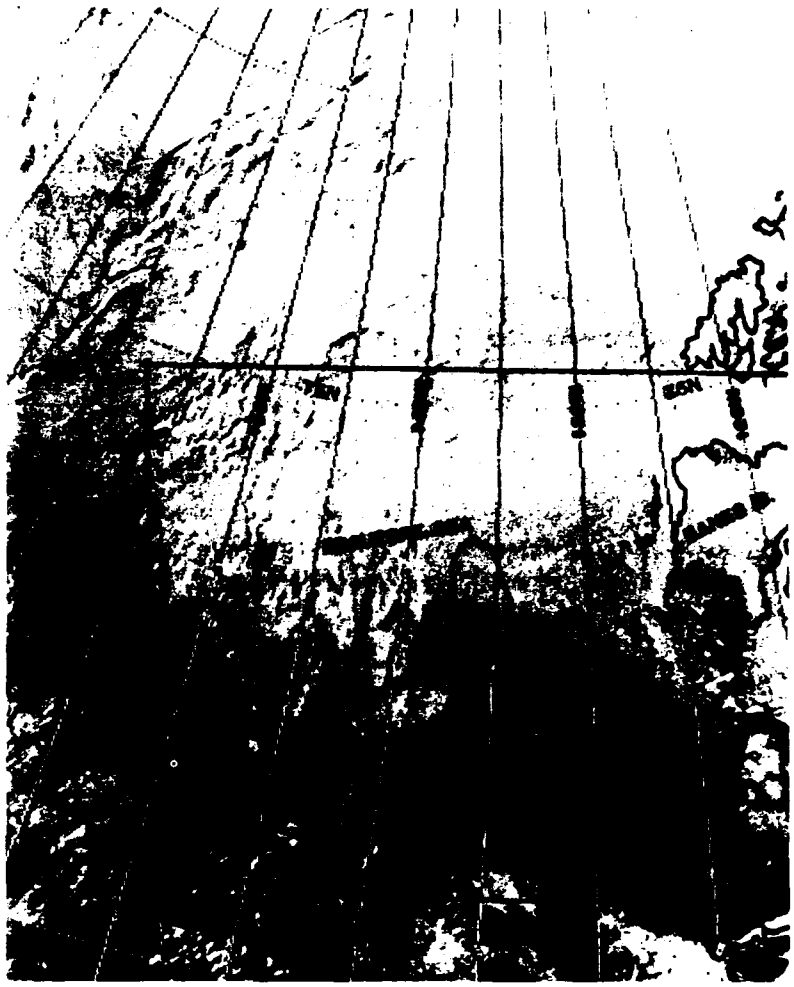

Figure 7. Overlay of sunglint pattern determined from 1536 UTC DMSP pass overlaid on image of figure 6.

The area of ice further west, from 130-140 W, appears more intact with almost complete ice cover. An overlay superimposed on this figure is shown as figure 7. The overlays displays the outline of a sun glint pattern observed over the ice in another DMSP visible image, acquired approximately three hours earlier, at 1536 UTC. This image is shown as figure 8. The area of sun glint is over the region of largely intact complete ice cover.

Sun glint also exposes flooded regions of the Mackenzie River delta. The Mackenzie River itself can be seen illuminated by sun glint in the lower right corner of the image. Interestingly, a portion of the band of ice curving around the mouth of the Mackenzie River delta is non-reflective, indicating a frozen surface not covered with liquid water, in contrast to the highly reflective, apparently flooded ice area to the north. This ice covered band may consist of less saline water from the Mackenzie River, which, having a higher melting point would remain frozen for a longer period.

Sun glint effects over water are now a well-known phenomena and have been described in many publications (Fett and Rabe 1976), chiefly relating to calm or rough water regions for either brilliant reflection, in the case of calm or nearly calm

seas or water, and reduced reflectance within a sun glint pattern for rough water regions. However, detection and interpretation of sun glint data over the ice-covered Arctic is a new topic, having received little or no previous attention.

The pattern observed in this example implies that the ice surface over the region of sun glint is largely covered by water. As the melt season progresses in the Arctic areas of flooded ice are commonly observed. Figure 1 is a photo of such a region (Courtesy of Defense Research Board, Canada—WMO/OMM/BMO—No 259, TP. 145). Although a considerable amount of ice exists in this image, these small elements would not be resolved in corresponding satellite imagery and their reflectivity would be averaged as part of the much more brilliant reflection from the surrounding water, creating an effect such as seen in figure 8

The possibility of a surface ice thaw associated with the development of surface brine layers is supported by meteorological data sets from Sachs Harbor, Banks Island, and Tutoyatuk, Northwest Territories, Canda. These data indicate an average temperature for Sachs Harbor of +1·7C and for Tutoyatuk of +6·0C during the period 1-18 June 1989. These temperatures are approximately 1-3C above normal for that time of year and would support an extensive melt condition, particularly in view of almost continuous daylight prevailing at the time.

Figure 8. DMSP visible image showing sunglint, 1536 UTC, 8 June 1989.

Additional insight concerning interpretation of effects in the area can be provided by an examination of the multi-channel AVHRR data of NOAA 10. Figure 9 shows the channel 4 infrared imagery obtained at 1738 UTC, less than an hour before the visible DMSP data of figure 6. The land surface of Alaska and Canada is dark grey or black, indicating temperatures warmer than that of the ice to the north. The land surface of Banks Island and Parry Peninsula is slightly colder than land temperatures further south and west. An area of snow south-east of the Parry Peninsula appears cold, emitting radiation at a temperature very similar to the temperature over the Beaufort Sea. The snow area can also be seen in figure 6.

The open water area or thin-covered ice region, apparent in the visible data in figure 6, appears in the infrared as a warmer band, extending northeastward from Herschel Island. NOAA-10 channel 1 visible data are shown in figure 10. These data show several ice features especially well, including large ice floes within the apparent open water area and a giant floe south of Banks Island. Note that the southern edge of the Beaufort Sea ice has a darker tone to it, indicative of a thinner ice condition. The channel 2 data of NOAA-10 (figure 11) are of special interest since the channel includes contributions from the near-infrared. Liquid water absorbs near-infrared radiation more strongly than visible radiation with the result that a darkening of the ice surface where melting has occurred is immediately apparent. This coincides almost perfectly with the sunlight region in figure 7.

The mid-IR channel of NOAA 10 is of additional interest. Figure 12 shows the channel 3 image of the region, inverted to show higher radiance values as white. Figure 13 is an enhancement of this image used to bring out detail in the ice cover. Channel 3 daytime imagery senses both scattered visible radiation and infrared thermal emission. Snow and ice surfaces and ice crystal clouds absorb strongly at this wavelength and appear black in the channel 3 image. Note that the ice floes and band of shore fast ice apparent in channel 1 data (figure 10) are almost invisible in

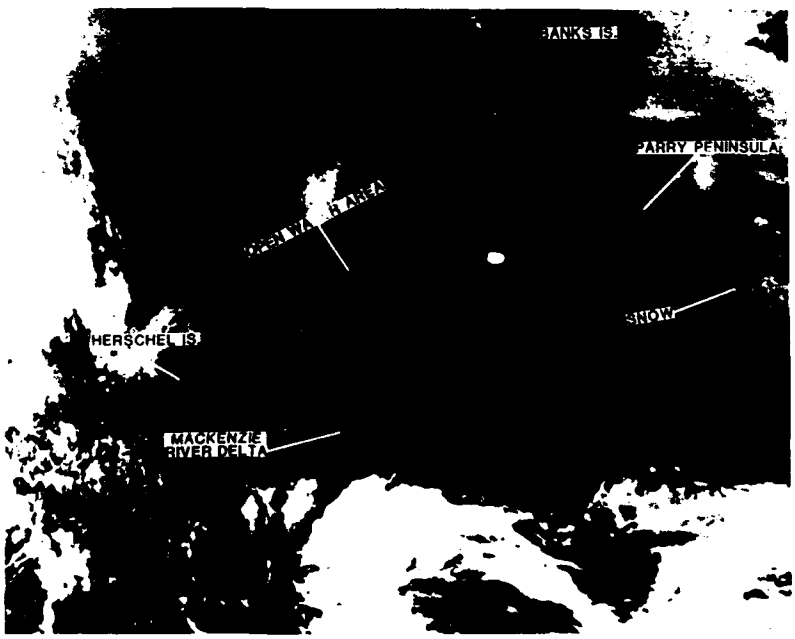

Figure 9. Channel 4 NOAA-10 image, 8 June 1989, 1730 UTC.

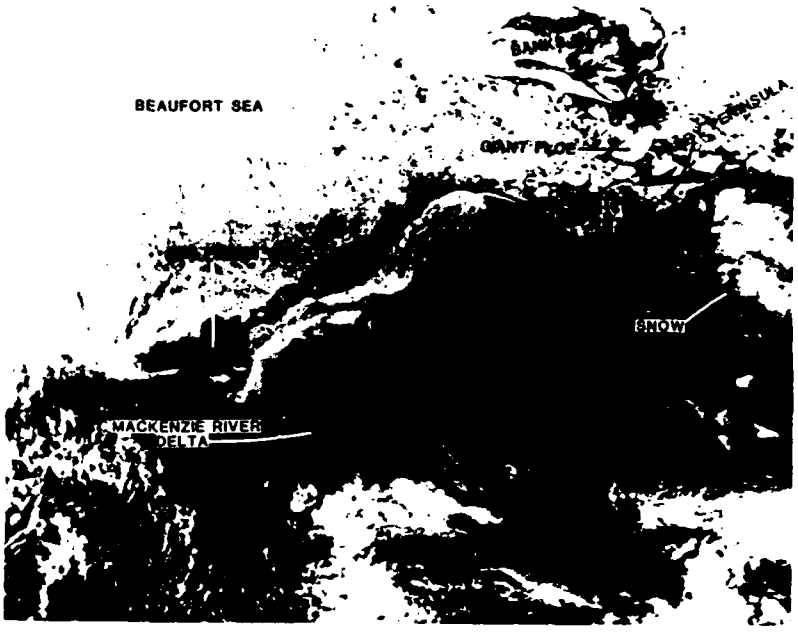

Figure 10. Channel 1 NOAA-10 image, 8 June 1989, 1730 UTC.

Figure 11. Channel 2 NOAA-10 image, 8 June 1989, 1730 UTC.

channel 3 (figure 12). In the enhanced image (figure 13) the open water area shows as a warmer region and the outline of the giant floe south of Banks Island can be faintly discerned because of heightened solar reflection.

Water areas outside the sunglint regions are essentially non-reflective and also appear dark when the air is cold. Hence most of the frozen ice, the water- covered ice, and the other open water areas, appear as dark grey or black, with little discrimination of differences. However, a cloud appears in the top centre of the image south-west of Banks Island and there is a patch of clouds just north-east of Herschel Island which are not particularly noticeable in either the visible NOAA channels, or in figure 6, the first DMSP image.

It is only when one carefully examines the second DMSP image (figure 8) that one can see that the grey shade intrusions into the sunglint to the west and east are, in fact, clouds or low fog obscuring underlying features of ice. The pattern of the cloud in the NOAA channel 3 data exactly duplicates the pattern of the grey shade intrusion from the east into the sunglint region of figure 8. The fact that this cloud and the cloudy patch north-east of Herschel Island cannot be seen with any distinction in any of the other visible band images indicates that the cloudiness is quite thin and essentially transparent at other viewing angles. Cloudiness extending over a sunglint area, however, immediately reduces the specular reflection from the region, making it easy to detect (Fett and Bohan 1977). These clouds are either very low level or perhaps surface fog, since the temperature of the clouds are virtually indistinguishable from the temperature of the surrounding ice as shown by the infrared data (figure 9).

7. Analysis of microwave imagery

The microwave data available for the analysis included only the 19, 22 and 37 GHz channels, with both polarizations in the first and third channels and only the

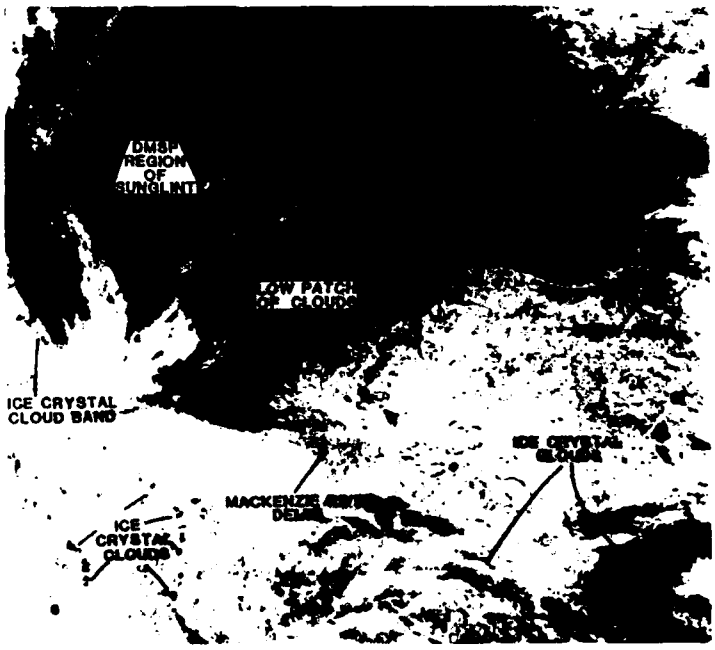

Figure 12. Channel 3 NOAA-10 image, 8 June 1989, 1730 UTC.

Figure 13. Enhancement of figure 11 to improve ice cover detail.

vertical channel in the second, water vapour channel. The high frequency channels of radiometer were noisy and not used. Both polarizations were initially examined, but the horizontal channels were found to be less useful in differentiating flooded and clear regions. This has been tentatively attributed to the horizontal channels' reflection of downwelling radiation.

The 19 GHz and 37 GHz vertically polarized channels were plotted against each other for the flooded region and its surroundings to see the occurrence of relationships expected from the theoretical analysis of the effect of flooding. Figure 14 shows that there seem to be several distinct regions in this scatter plot. The

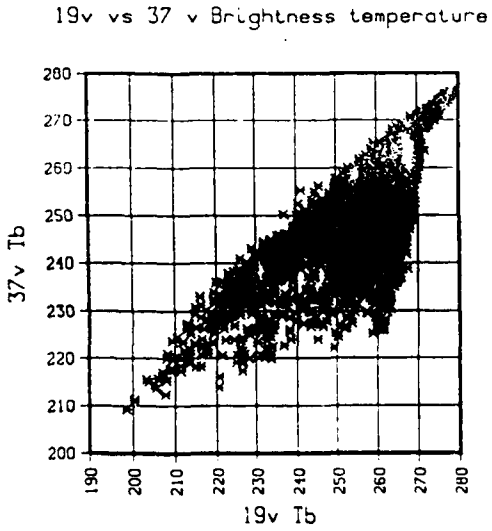

Figure 14. Plot of Channel 1 (19 GHz vertical) versus Channel 4 (37 GHz vertical), 8 June 1989 UTC for region bounded by 74° N, 140° W, and 70° N, 120° W.

majority of the points lie along the diagonal, indicating the two channels are linearly dependent with a slope near unity. Several other relatively distinct regions show a substantially different, increased slope. The sign and size of the slope indicates there is more variance associated with the higher frequency channel than the lower frequency channel. This is consistent with the inference from figure 7 that some flooding may exist.

The scatter plot was separated into several different regions for detailed comparison with the optical satellite observations. By trial and error, it was found that a area 1° in latitude by 2·5° in longitude provided sufficient data for analysis of the distribution of observations, without excessive mixing of ice type within an analysis box. Smaller areas, while providing more uniform surface conditions presented too few pixels for determination of a distribution with any confidence.

A region of well-defined surface flooding is shown in figure 15(*a*) which shows the scatter plot for the region bounded by 72 N, 132·5 W and 73 N, 130 W. In this region, the 19 GHz temperature varies by more than 15°, while the 19 GHz V channel varies by less than 3°. From the optical analysis, this region is associated with the surface melt, although there is some cloud cover in parts of the area.

Farther east, the scatter plot shows similar behaviour, although not as well differentiated as in the first region. Figure 15(*b*) the scatter plot for the region bounded by 73 N, 130 W and 72 N, 127·5 W, shows a 19 GHz temperature range of 9°, with a 37 GHz temperature range of 18°. The optical imagery indicates that flooding is potentially present, but there also is some lead formation in the area. The areas of open water are expected to have a similar effect on the distribution of both channel temperatures, thus resulting in a larger range than in the previous region.

Still farther east, the ice breakup becomes more marked. This is also seen in figure 15(*c*) (between 72 N, 122·5 W and 72 N, 125 W), where the range of both frequency channels are similar to that of figure 15(*b*). It is interesting that there is a slight amount of land contamination by Banks Island, but the general behaviour does not change.

An area characterized by broken ice, with a similar fraction of deep water (relative to the microwave skin depth) and ice cover is seen in figure 15(*d*) (between 71 N, 135 W and 70 N, 132·5 W). The scatter plot show a definite linear relation of the 19 V to 37 V channels, quite different from the regions earlier. This behaviour can be attributed to the averaging of large fairly uniform areas of ice and water. The water regions are probably greater than several centimetres in depth, and should extend over regions the size of an SSM/I footprint, 25 km^2.

8. Conclusions

A two component radiance model of the microwave emissivity of a flooded ice surface is presented to explain the behaviour of a microwave signal over polar ice regions. The model provides a relationship of the frequency dependent brightness temperature and the depth of the surface brine layer.

Simultaneous visible and microwave imagery of the Arctic ice pack have been presented for a region of flooded ice in the Beaufort Sea on 8 June, 1989. Analysis of visible and infrared imagery from DMSP OLS and NOAA-10 AVHRR sensors demonstrate varying surface conditions, including new ice cover, multi-year ice, and flooded ice regions.

The corresponding microwave brightness temperature imagery provides a qualitative estimate of the depth of the overlying brine layer. We have found that areas of

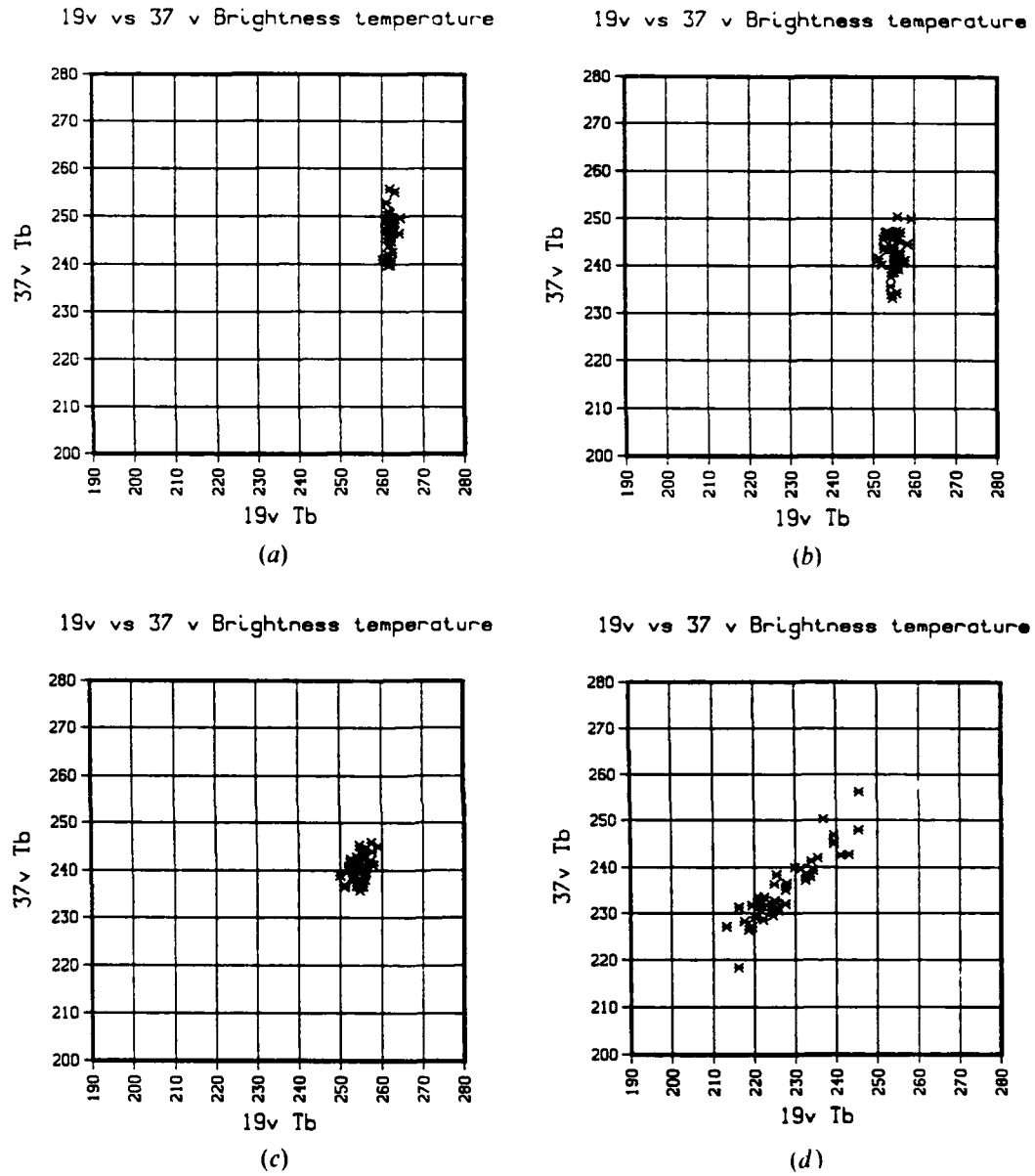

Figure 15(*a*) Plot of Channel 1 (19 GHz vertical) versus Channel 4 (37 GHz vertical), 8 June 1989 UTC for region bounded by 72° N, 132·5° W, and 73° N, 130° W. (*b*) Plot of Channel 1 (19 GHz vertical) versus Channel 4 (37 GHz vertical), 8 June 1989 UTC for region bounded by 73° N, 130° W, and 72° N, 127·5° W. (*c*) Plot of Channel 1 (10 GHz vertical) versus Channel 4 (37 GHz vertical), 8 June 1989 UTC for region bounded by 72° N, 122·5° W, and 72° N, 125° W. (*d*) Plot of Channel 1 (19 GHz vertical) versus Channel 4 (37 GHz vertical), 8 June 1989 UTC for region bounded by 71° N, 135° W, and 70° N, 132·5° W.

approximate 1° latitude by 2·5° in longitude are a reasonable compromise between retrieving a sufficient number of pixels, and having a uniform surface area. The brightness temperature of the higher frequency channels within these sub-regions varied as expected, with wider range of high frequency than low frequency T_b values in the flooded regions. This frequency dependence of the brine layer indicates that

the liquid layer is present, but is only 1 cm or less in thickness. In regions where there is evidence of ice breakup in addition to the flooding, this behaviour of the frequency dependence does not seem to be affected by the flooding. Averaging the behaviour of ice and open water areas seems to explain the observed behaviour.

The characterization of the multi-spectral surface emissivity by its spatial variation implies that textural analysis may be a useful tool for analysis of polar surface observations. The current use of spectral variation of the microwave could be supplemented by spatial texture analysis to differentiate among ice types. Further development of these tools require a more extensive data set than currently available.

References

BORN, M., and WOLF, E., 1965, *Principles of Optics*, 2nd Edition (Oxford: Pergamon Press).

CAVALIERI, D. J., MARTIN, S., and GLOERSON, P., 1983, Nimbus 7 SMMR observations of the Bering Sea ice cover during March 1979. *Journal of Geophysical Research*, **88** 2743-2754.

COMISO, J. C., 1983, Sea ice effective microwave emissivities from satellite passive microwave and infrared observations. *Journal of Geophysical Research*, **88**, 7686-7704.

COMISO, J. C., ACKLEY, S. F., and GORDON, A. L., 1984, Antarctic Sea ice microwave signatures and their correlation with *in situ* ice observations. *Journal of Geophysical Research*, **89**, 662-772.

FETT, R., and BOHAN, W. J., 1977, Navy Tactical Applications Guide (NTAG), Volume 1, Techniques and applications of image analysis, Naval Environmental Prediction Research Facility Technical Report 77-03, Monterey, CA.

FETT, R., and RABE, K., 1976, Island barrier effects on sea state as revealed by a numerical model and meteorological satellites. *Journal of Physical Oceanography*, **6**, 324-334.

GARRITY, C., RAMSEIER, R. O., and RUBINSTEIN, I. G., 1990, Snow wetness and SSM/I brightness temperatures for the Weddell Sea. *Proceedings of the 10th International Geoscience & Remote Sensing Symposium, College Park MD, Volume 2*, (New York: Institute of Electrical and Electronic Engineers), pp. 1521-1524.

GRODY, N., 1988, Surface identification using satellite microwave radiometers. *I.E.E.E. Transactions on Geoscience and Remote Sensing*, **26**, 850-859.

HOLLINGER, J., R. LO, G. POE, R. SAVAGE, and J. PEIRCE, 1987, *Special Sensor Microwave/Imager User's Guide* (Washington, DC: Naval Research Laboratory).

ISAACS, R. G., JIN, YA-QUI, WORSHAM R. D., DEBLONDE, G., and FALCONE, V. J. JR, 1989, The RADTRAN microwave surface emission models. *I.E.E.E. Transactions—Geoscience and Remote Sensing*, **25**, 433-440.

SIMMER, C., REPRECHT, E., and WAGNER, D., 1989, The influence of the vertical structure of humidity on the retrieval of total water vapour content over the oceans by microwave radiometry from space. In *Microwave Remote Sensing of the Earth System*, edited by A. Chedin, (Hampton, VA: A. Deepak Publishing), pp. 75-94.

STOGRYN, A., 1971, Equations for calculating the dielectric constant of saline water. *Transactions—Microwave Theory and Technology*, **MIT-19**, 733-736.

SVENDSEN, E., KLOSTER, K., FARRELLY, B., JOHANNESSEN, O. M., JOHANNESSEN, J. A., CAMPBELL, W. J., GLOERSEN, P., CAVALIERI, D., and MATZLER, C., 1983, Norwegian Remote Sensing Experiment: Evaluation of the Nimbus 7 Scanning Multichannel Microwave Radiometer for sea ice research. *Journal of Geophysical Research*, **88**, 2781-2791.

ULBAY, F. T., MOORE, R. K., and FUNG, A. K., 1986, *Microwave Remote Sensing: Active and Passive*, Volume III (Norwood, MA: Artech House).

Appendix A

Microwave absorption of brine

This appendix provides the parametrizations used to compute the microwave absorption coefficients used in the calculation of effective brightness temperatures above a liquid water surface.

The absorption coefficient is related to the complex permittivity of the material,

$$k=\frac{2\pi}{\lambda_0}Im\sqrt{\varepsilon} \tag{A1}$$

where λ_0 is the free space wavelength of the incoming radiation and ε is the complex dielectric coefficient. The complex dielectric coefficient depends on the physical characteristics of the material by the Debye relaxation formula (Born and Wolf, 1965),

$$\varepsilon=\varepsilon'-j\varepsilon'' \tag{A2}$$

where j is the square root of -1, and the real part of the relaxation coefficient is given by

$$\varepsilon'=\varepsilon_{SW\infty}+\frac{\varepsilon_{sw0}-\varepsilon_{SW\infty}}{1+(2\pi f\tau_{sw})^2} \tag{A3}$$

$$\varepsilon''=\frac{2\pi f\tau_{sw}(\varepsilon_{sw0}-\varepsilon_{sw\infty})}{1+2\pi f\tau_{sw}}+\frac{\sigma_i}{2\pi\varepsilon_0 f} \tag{A4}$$

where f is the frequency (Hz), τ_{sw} is the relaxation time of the solution (sec), ε_0 is the permittivity of free space ($8{\cdot}855\times10^{-12}\,\mathrm{F\,m^{-1}}$) and $\varepsilon_{sw\infty}$ is the static permittivity (4·9). We use the parametrizations of Stogryn (1971) relating ε_{sw} *to the salinity* S(0/00) and the temperature T(C) by

$$\varepsilon_{sw0}(T,S)=\varepsilon_{sw0}(T,0)\,a(T,S) \tag{A5}$$

where

$$\varepsilon_{sw0}(T,0)=87{\cdot}134+(-0{\cdot}1949+(-0{\cdot}01276+0{\cdot}0002491\,T)\,T)\,T \tag{A6}$$

The relaxation time is parameterized by also separating the salinity dependence

$$a(T,S)=1+0{\cdot}613\times10^{-5}\,TS+(-3{\cdot}656\times10^{-3}+(3{\cdot}210\times10^{-5}-4{\cdot}232\times10^{-7}\,S)\,S)\,S \tag{A7}$$

$$\tau_{sw}(T,S)=\tau_{sw}(T,0)\,b(T,S_{sw}) \tag{A8}$$

$$2\pi\tau_{sw}(T,0)=1{\cdot}1109\times10^{-10}+(-13{\cdot}824\times10^{-12}+(0{\cdot}6938\times10^{-14}-5{\cdot}096\times10^{-16}T)T)T \tag{A9}$$

$$b(T,S)=1+2{\cdot}282\times10^{-5}TS+(-7{\cdot}638\times10^{-4}+(-7{\cdot}76\times10^{-6}+1{\cdot}105\times10^{-8}S)S)S \tag{A10}$$

The ionic conductivity is separated into a salinity and temperature dependence as

$$\sigma_i(T,S)=\sigma_i(25,S)e^{-\phi} \tag{A11}$$

where σ_i (25,S) is the ionic conductivity of sea water at 25 C and is given by

$$\sigma_i(25,S)=(0{\cdot}1852+(-0{\cdot}0014619+(2{\cdot}093\times10^{-5}-1{\cdot}282\times10^{-7}\,S)\,S)\,S)\,S \tag{A12}$$

The function ϕ depends on S and $\Delta = 25 - T$

$$\phi = (0{\cdot}02033 + (1{\cdot}266 \times 10^{-4} + 2{\cdot}464 \times 10^{-6}\Delta)\Delta - (1{\cdot}849 \times 10^{-5} - 2{\cdot}551 \times 10^{-7} + 2{\cdot}551 \times 10^{-8}\Delta)\,\Delta)\,\Delta)\,\Delta S \tag{A13}$$